

Tomography of the low excitation planetary nebula NGC 40

F. Sabbadin¹, E. Cappellaro¹, S. Benetti³, M. Turatto¹, and C. Zanin^{2,4}

¹ Osservatorio Astronomico di Padova, vicolo dell'Osservatorio 5, I-35122 Padova, Italy

² Dipartimento di Astronomia, Università di Padova, vicolo dell'Osservatorio 5, I-35122 Padova, Italy

³ Telescopio Nazionale Galileo, Aptdo. Correos 565, E-38700 Santa Cruz de la Palma, Canary Island, Spain

⁴ Institut für Astronomie der Leopold-Franzens-Universität Innsbruck, Technikerstraße 25, A-6020 Innsbruck, Austria

Received; accepted

Abstract. Spatially resolved, long-slit echellograms at different position angles of the bright, low excitation planetary nebula NGC 40 indicate that, the higher is the gas excitation, the faster is the radial motion, thus confirming the overturn of the Wilson law already suggested by Sabbadin and Hamzaoglu (1982).

New reduction procedures, giving the radial trends of the electron density and of the ionic and chemical abundances, were applied to NGC 40; they show that:

- the radial matter distribution has a sharp “bell” profile with peaks up to 4000 cm^{-3} ;
- the ionization structure is peculiar, indicating the presence of chemical composition gradients within the nebula: the innermost regions, hydrogen depleted, are essentially constituted of photospheric material ejected at high velocity by the WC8 nucleus.

Moreover, detailed H^+ , O^{++} and N^+ tomographic maps, giving the spatial ionic distributions at four position angles, are presented and discussed within the interacting winds evolutionary model.

Key words: planetary nebulae: individual: NGC 40 – ISM: kinematics and dynamics – ISM: abundances

1. Introduction

NGC 40 (PNG120.0+09.8, Acker et al., 1992; Figure 1) is a very low excitation planetary nebula powered by a WC8

Send offprint requests to: F. Sabbadin

Fig. 1. Broad-band R image of NGC 40 (exposure time 180s, seeing $0.85''$) obtained with the 3.5m Italian National Telescope (TNG), revealing the intricate $\text{H}\alpha$ + $[\text{NII}]$ nebular structure. North is up and East is on the left.

star presenting a mass-loss rate of the order of $10^{-6} - 10^{-8} M_{\odot} \text{ yr}^{-1}$ with wind velocities between 1800 and 2370 km s^{-1} (Cerruti-Sola and Perinotto, 1985; Bianchi, 1992).

The nebula is described by Curtis (1918) as a truncated ring, from the end of which extend much fainter wisps; the brighter central portion is $38 \times 35''$ in $\text{PA}=14^{\circ}$, while the total length along this axis is about $60''$. Deep, narrow-band imagery by Balick et al. (1992) reveals the presence of an external network of knotty floccules and smooth filaments. Meaburn et al. (1996) identify two haloes around the barrel-shaped core, and a jet-like feature projecting from it.

Detailed low resolution spectroscopy (Aller and Czyzak, 1979, 1983; Clegg et al., 1983) indicates point to point changes of the excitation and chemical abundances which are typical of planetary nebulae, without apparent contamination by the fast stellar wind.

A kinematical analysis secured by Sabbadin and Hamzaoglu (1982) suggests the presence of peculiar motions in the central part of NGC 40, with the expansion velocity larger in $[\text{OIII}]$ than in $\text{H}\alpha$ and $[\text{NII}]$.

More recently, Meaburn et al. (1996) obtained long-slit $\text{H}\alpha$ and $[\text{NII}]$ high resolution spectra of the bright core, of the two haloes and of the jet-like feature. These authors showed that the outer filamentary halo is practically inert and that the motion of the inner, diffuse, spherical halo mimics the one observed over the bright nebular core; moreover, the jet-like structure is kinematically associated with the receding end of the barrel shaped-core and does not present any of the characteristics expected of a true jet.

In order to study in detail the nebular physical conditions and to apply an original procedure giving the spatial matter distribution along the cross-section covered by the spectroscopic slit, on December 1998 we obtained a number of echellograms at different position angles of a dozen of winter planetary nebulae (NGC 40, 650-1, 1501, 1535, 2022, 2371-2, 2392, 7354 and 7662, J 320 and 900, A 12 and M 1-7).

In this paper we report the results derived for NGC 40. In Section 2 we present the observational material; in

Section 3 we discuss the expansion velocity field; in Section 4, the electron temperature and the electron density are analysed and a new method to determine the radial distribution of the electron density in expanding nebulae is presented. The radial ionization structure of NGC 40 is given in Section 5 and the resulting chemical composition gradients in Section 6. Section 7 shows the H^+ , O^{++} and N^+ tomographic maps derived at four position angles; a short discussion is contained in Section 8 and conclusions are drawn in Section 9.

2. Observational material

Broad-band U, V and R imagery of NGC 40 was obtained with the Optical Imager Galileo (OIG) camera mounted on the Nasmyth A adapter interface (scale= $5.36'' \text{ mm}^{-1}$) of the 3.5m Italian National Telescope (TNG, Roque de los Muchachos, La Palma, Canary Islands). The OIG camera was equipped with a mosaic of two thinned and back-illuminated EEV42-80 CCDs with 2048×4096 pixels each (pixel size= 13.5 microns ; pixel scale= $0.072'' \text{ pix}^{-1}$).

Though these images were taken during the testing period of the instrument (when interference filters were unavailable), they reveal new morphological details of the nebula supporting our spectroscopic results and will be presented later-on (Section 5).

Spatially resolved, long-slit spectra of the bright core of NGC 40 in the range $\lambda\lambda 4500\text{-}8000 \text{ \AA}$ (+flat fields+Th-Ar calibrations+ comparison star spectra) were obtained with the Echelle spectrograph (Sabbadin and Hamzaoglu, 1981, 1982) attached to the Cassegrain focus of the 182cm Asiago telescope, combined with a Thompson 1024×1024 pixels CCD.

Four position angles were selected: 20° (apparent major axis), 110° (apparent minor axis), 65° and 155° (intermediate positions). In all cases the slit-width was 0.200 mm ($2.5''$ on the sky), corresponding to a spectral resolution of 13.5 km s^{-1} (1.5 pixel). During the exposures the slit grazed the bright central star (we tried to avoid most of the continuum contamination; the faint stellar spectrum present in our echellograms was used as reference for the nebular centre and to correct the observations for seeing and guiding errors).

All spectra were calibrated in wavelength and flux in the standard way using the IRAF data reduction software.

The following nebular emissions were detected: $H\beta$, $\lambda 4959 \text{ \AA}$ and $\lambda 5007 \text{ \AA}$ of [OIII], $\lambda 5755 \text{ \AA}$ of [NII], $\lambda 5876 \text{ \AA}$ of HeI, $\lambda 6300 \text{ \AA}$ and $\lambda 6363 \text{ \AA}$ of [OI] (the first at the order edge; both partially blended with night-sky lines), $\lambda 6548 \text{ \AA}$ and $\lambda 6584 \text{ \AA}$ of [NII], $H\alpha$, $\lambda 6578 \text{ \AA}$ of CII, $\lambda 6717 \text{ \AA}$ and $\lambda 6731 \text{ \AA}$ of [SII], $\lambda 7135 \text{ \AA}$ of [ArIII], $\lambda 7320 \text{ \AA}$ and $\lambda 7330 \text{ \AA}$ of [OII] (at the extreme edge of the order; out of focus) and $\lambda 3726 \text{ \AA}$ and $\lambda 3729 \text{ \AA}$ of [OII] (second order).

All line intensities (but not the second order doublet of [OII]) were de-reddened by fitting the observed $H\alpha/H\beta$ ratio to the one computed by Brocklehurst (1971) for

$Te=10^4 \text{ K}$ and $Ne=10^4 \text{ cm}^{-3}$. We derive a logarithmic extinction at $H\beta$, $c(H\beta)=0.60 \pm 0.10$, to be compared with the values of 0.28, 0.65 and 0.70 obtained by Kaler (1976), Aller and Czyzak (1979) and Clegg et al. (1983), respectively. The fair agreement (within 10%) between our integrated line intensities and those reported in the literature from low resolution spectra (see, for example, Clegg et al., 1983) induced us to adopt $I(3726+3729)/I(H\alpha)=1.48$, as reported by these authors.

A large variety of emission structures is present in NGC 40; for illustrative purposes, some examples are given in Figure 2. In these reproductions the faint stellar continuum was removed and the observed intensities enhanced (by the factor given in parenthesis) to make each line comparable with $H\alpha$.

Our spectra at $PA=110^\circ$ (apparent minor axis, Fig. 2a) were centred $2''$ South of the central star. All emissions present the classical bowed shape expected for expanding shells of different mean radii r and thicknesses t , ranging from $r = 16''$ for [OIII] and CII to $r = 19''$ for [NII] and [SII] and from $t = 0.20r$ for [NII] and [SII] to $t = 0.25r$ for [OIII] and CII (as also suggested by the integral intensity distributions along the slit).

At $PA=20^\circ$ (apparent major axis; slit centre $2''$ West of the star; Fig. 2b) low excitation lines (such as the [SII] red doublet) show knotty structures and fail to close at either polar cap. High excitation emissions (for instance [OIII]) appear more homogeneous; they merge in a diffuse zone internal to the polar caps; the smooth intensity distribution and the large velocity spread suggest that [OIII] completely fills this part of nebula; moreover, the faintness (or absence) of an external low excitation counterpart indicates that in these directions the main body of NGC 40 is density bounded rather than ionization bounded.

Spectra taken at $PA=65^\circ$ (Fig. 2c) were centred $2''$ S-E of the central star; they appear quite regular, but for a deformation of the blue-shifted component in the E-NE quadrant.

At $PA=155^\circ$ (centre of the slit $2''$ S-W of the star; Fig. 2d) low excitation lines (such as the [NII] line at $\lambda 6584 \text{ \AA}$) merge in the N-NW sector, in correspondence of a bright knot. The S-SE region is strongly depauperated of gas and only high excitation emissions (like the extremely faint CII line at $\lambda 6578 \text{ \AA}$) present a close structure; as already seen for $PA=20^\circ$, the weakness of external low excitation emissions suggests that in these directions the nebula is density bounded.

3. The expansion velocity field

First of all we measured the peak separation at the centre of each nebular emission. Results are presented in Table 1, where ions are put in order of increasing ionization potential.

We find a complete overturn of the Wilson law: in NGC 40 the higher is the ionization, the faster is the motion

Fig. 2. Representative examples of emission line structures observed in NGC 40 at different position angles. Each line intensity was multiplied by the factor given in parenthesis to make it comparable with $H\alpha$.

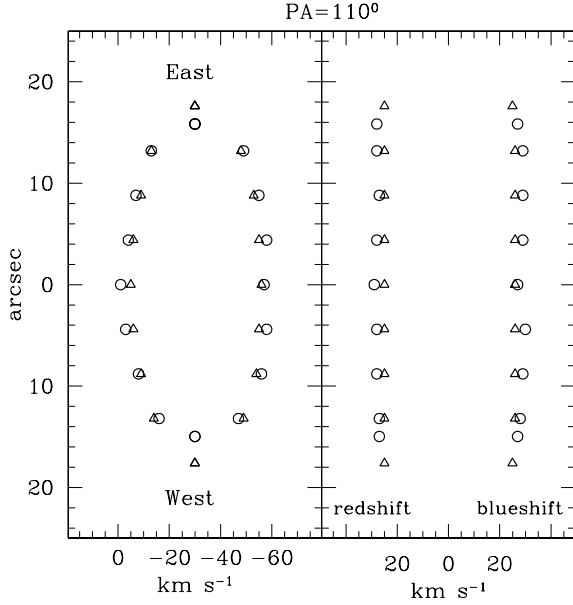


Fig. 3. Observed (left panel) and deprojected (right panel) expansion velocity field at $PA=110^\circ$ (apparent minor axis). Triangles are for [NII] and circles for [OIII].

Table 1. Expansion velocities

λ (\AA)	ion	I.P. (eV)	$2V_{exp}$ (km s^{-1})	notes
6300	[OI]	0	51 ± 2	1
6717-6731	[SII]	10.4	51 ± 2	
6563	HI	13.6	50 ± 1	
3726-3729	[OII]	13.6	54 ± 2	2
6584	[NII]	14.5	51 ± 1	
6578	CII	24.4	53 ± 2	
5876	HeI	24.6	53 ± 2	
7135	[ArIII]	27.6	54 ± 2	
5007	[OIII]	35.1	57 ± 1	

1 = partially blended with night-sky emission
 2 = second order lines

(thus confirming the suggestion by Sabbadin and Hamzaoglu, 1982, of a peculiar [OIII] expansion velocity).

A further peculiarity is represented by [OII], which expands faster than the other low ionization species. This [OII] velocity-excess is related to the very low degree of

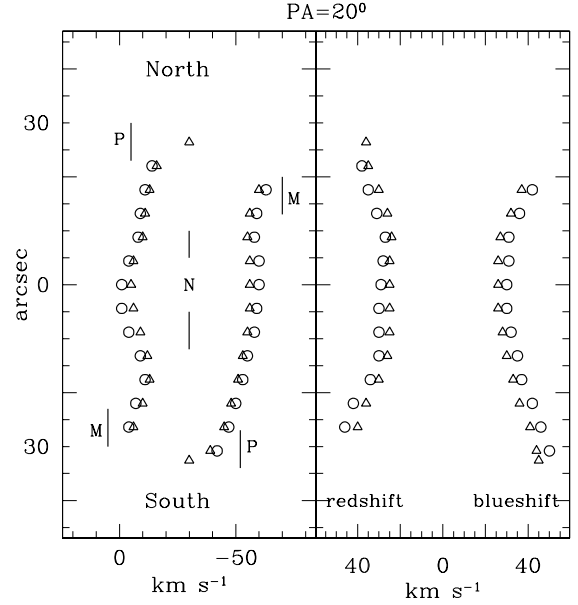


Fig. 4. Same as Fig. 3, but for $PA=20^\circ$ (apparent major axis). Glossary: N=main nebula, P=polar caps (blue-shifted at south, red-shifted at north), M=extremely faint $H\alpha$ and [NII] mustaches (red-shifted at south, blue-shifted at north) emerging from the main nebular body.

excitation of the nebula: since the O^+ zone stops at 35.1 eV (while, for example, S^+ falls at 23.4 eV and N^+ at 29.6 eV), it extends well inwards, as also indicated by the [OIII] weakness. So, in NGC 40, [OII] must be considered a medium-high excitation species (at least for the dynamical point of view).

Clearly, the expansion velocities reported in Table 1 are only mean values and do not describe the complex kinematics of the nebula. To better illustrate this, we have selected two position angles (110° =apparent minor axis; 20° =apparent major axis) and chosen [NII] for low excitation regions and [OIII] for the high excitation ones ("high" at least for NGC 40!).

The regular ellipses shown by these ions at $PA=110^\circ$ (Figure 3, left panel) are typical of expanding shells; the absence of tilt indicates that the nebular cross-sections are either circular, or elliptical (in this second case we are aligned with one of the axes). In fact, the de-projection of the observed expansion velocities (assuming a simple,

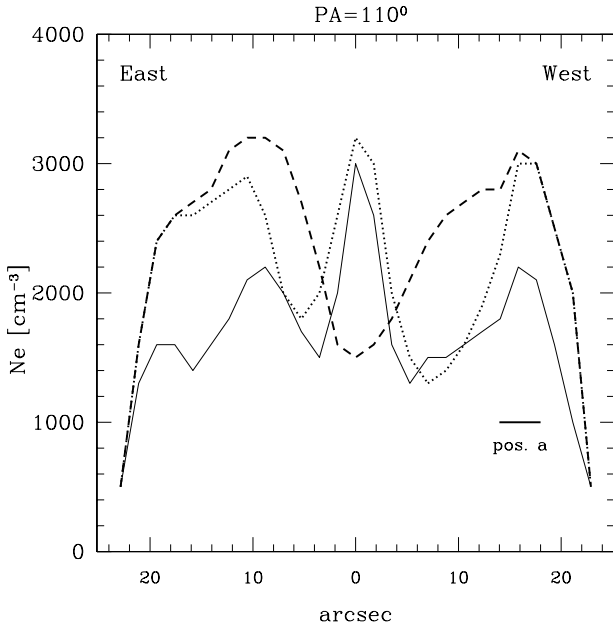


Fig. 5. [SII] electron density trends observed at PA=110° for the blue-shifted (dotted curve) and red-shifted (dashed curve) peaks and for the integrated spectrum (solid curve). “Position a” of Clegg et al. (1983) is indicated.

direct position-speed correlation) gives the “true” expansion velocities presented in the right panel of Figure 3, i.e. a constant value for each ion. Similar trends are obtained also at PA=65° and in the N-NW sector of PA=155°.

The [NII] and [OIII] expansion velocity fields observed at PA=20° (major axis) are given in Figure 4 (left panel). Here the situation is more complicated, mainly with respect to [OIII]. In fact, while [NII] presents sharp emissions along the slit, [OIII] describes an ellipse which is well defined in the main part of the nebula, but becomes smooth and broad to the north and south. The de-projection of the observed velocities (right panel of Figure 4) points out the acceleration suffered by the polar (less dense) nebular material. A similar behavior occurs at PA=155°, in the S-SE sector.

For a better understanding of the peculiar kinematics of NGC 40, a detailed analysis of the nebular physical conditions can be useful.

4. Electron temperature (T_e) and electron density (N_e)

The only T_e diagnostic present in our spectra is the line intensity ratio 6584/5755 Å of [NII]. Unfortunately, the auroral emission is too weak for a detailed analysis; for the brightest parts of NGC 40 we obtain $I(6584)/I(5755)=125\pm 20$, corresponding to $T_e=7900\pm 200$ K (assuming $N_e=10^4$ cm⁻³). Thus, according to Aller and Czyzak (1979, 1983) and Clegg et al. (1983),

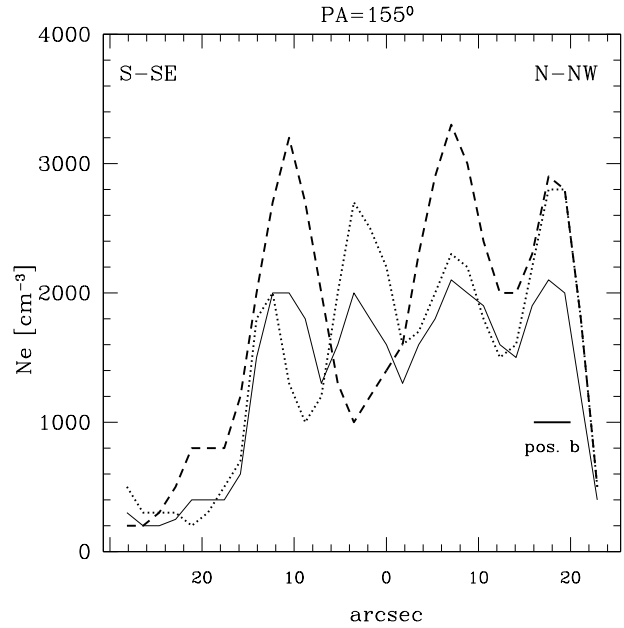


Fig. 6. Same as Fig. 5, but for PA=155°. “Position b” of Clegg et al. (1983) is indicated.

we will adopt $T_e=8000$ K for low ionization regions (O^0 , N^+ , S^+ , O^+) and $T_e=10000$ K for the others (O^{++} , He^+ , C^+ , Ar^{++}).

Our N_e study is essentially based on [SII] lines at $\lambda 6717$ Å and $\lambda 6731$ Å.

To test the reliability of our measurements we can make a comparison with the results of Clegg et al. (1983), who observed at low spectral resolution a patch of nebuleosity located at north-west of the central star. At “position a” they found $I(6717)/I(6731)=0.68$, corresponding to $N_e=2200$ cm⁻³ (for $T_e=8000$ K). “Position a” practically coincides with the bright western edge of our spectra taken at PA=110° (apparent minor axis).

The [SII] density distribution we observed at this position angle is shown in Figure 5 for the blue-shifted and the red-shifted peaks, and also for the integrated, low resolution spectrum (we have averaged our echellograms over a velocity range of 312 km s⁻¹, which corresponds to the spectral resolution used by Clegg et al., 1983). The estimated N_e accuracy varies from $\pm 15\%$ for high density peaks (generally -but not always- coinciding with the strongest emissions), to $\pm 50\%$ for deep valleys (weakest components).

For “position a” the integrated spectrum gives $N_e=2100$ cm⁻³, in good agreement with Clegg et al. (1983), but high resolution measurements indicate a density of 3100 cm⁻³. Note that in Figure 5 the maximum density of the integrated spectrum (3000 cm⁻³) is reached in a relatively weak knot projected onto the central star; it corresponds to a peak (3200 cm⁻³) in the blue-shifted component.

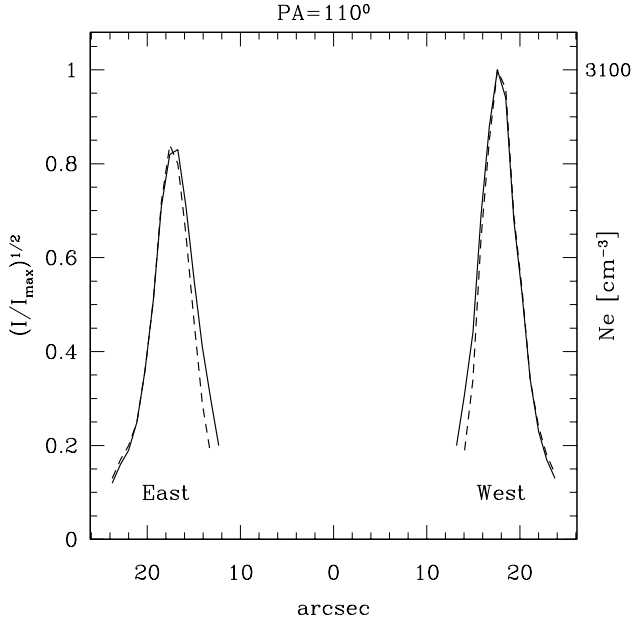


Fig. 7. Relative (left ordinate scale) and absolute (right ordinate scale) radial electron density distributions at $PA=110^\circ$ from the $H\alpha$ (solid curve) and $[NII]$ (dashed curve) zero-velocity columns.

As a further example, in Figure 6 we present the $[SII]$ density distribution observed at $PA=155^\circ$; symbols are as in Figure 5. In this case our N-NW peak is partially superimposed to “position b” of Clegg et al. (1983). Once again their electron density ($Ne=2100 \text{ cm}^{-3}$) coincides with our integrated value, but is considerably lower than the peak measured at high resolution ($Ne=2900 \text{ cm}^{-3}$).

CAVEAT: *strictly speaking, our Ne estimates too must be considered as lower limits, due to ionization effects. In fact, as we will see in the next section, the complete recombination of S^{++} occurs externally to the top of the density distribution; this implies that the peak of the $[SII]$ intensity distribution is slightly outwards with respect to the density maximum, leading to a small underestimate of Ne derived from the $[SII]$ line intensity ratio.*

Besides the density peak along the cross-section of the nebula, our high resolution spectra allow to derive the radial distribution of the electron density using the “zero-velocity column” of each emission line; this is the central, rest-frame pixel column containing the ionized gas moving in the neighborhood of -30 km s^{-1} (mean radial velocity of the whole nebula). In practice, the zero-velocity column contains the material which is expanding normally to the line of sight; it is important because it insulates a definite slide of nebula which is unaffected by the expansion velocity field.

The intensity distribution observed in the zero-velocity column of each nebular emission must be cleaned of the broadening effects due to:

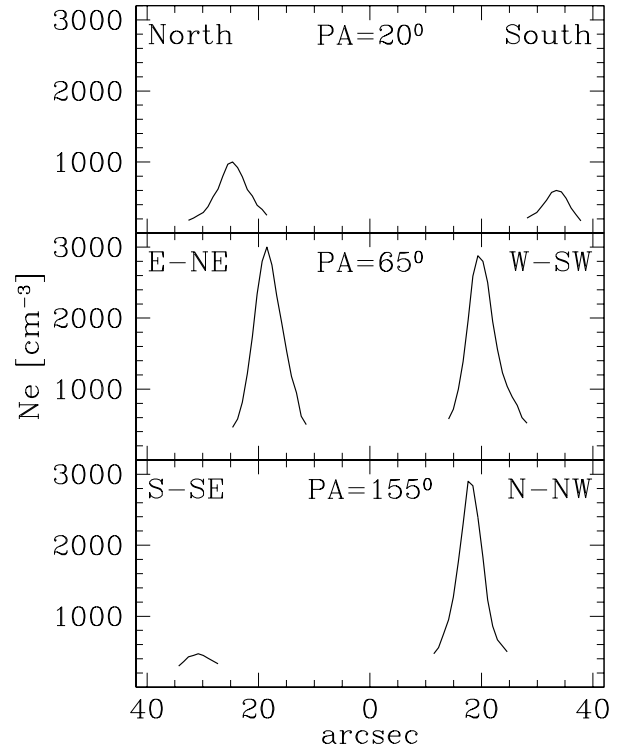


Fig. 8. Radial electron density profiles obtained from the $H\alpha$ zero-velocity columns at $PA=20^\circ$, 65° and 155° .

- instrumental profile, corresponding to a Gaussian having $FWHM=13.5 \text{ km s}^{-1}$;
- thermal motions; for $Te=8000 \text{ K}$ they amount to 19 km s^{-1} for H, 9.5 km s^{-1} for He and 5 km s^{-1} (or less) for the heavier elements;
- turbulent motions, which affect all lines in the same way; following Meaburn et al. (1996) in NGC 40 they are $6 - 8 \text{ km s}^{-1}$;
- fine structure of $H\alpha$ and $\lambda 5876 \text{ \AA}$ of HeI. Following Dyson and Meaburn (1971) and Dopita (1972), the seven $H\alpha$ components can be shaped as the sum of two equal Gaussian profiles separated by 0.14 \AA . $\lambda 5876 \text{ \AA}$ of HeI has six components: five of them are concentrated in the narrow range $\lambda\lambda 5875.5987 - 5875.6403 \text{ \AA}$ (they were considered a single emission at $\lambda 5875.62 \text{ \AA}$); the sixth one, located at $\lambda 5875.9663 \text{ \AA}$, is 4.4 times weaker (and then it was neglected).

We have derived the corrected intensity of the zero-velocity columns by deconvolving the observed profile at any given nebular position along the slit into a series of Gaussians spaced of one pixel along the dispersion and having: $FWHM=25.8 \text{ km s}^{-1}$ for $H\alpha$, 17.9 km s^{-1} for $\lambda 5876 \text{ \AA}$ of HeI and $FWHM=16.0 \text{ km s}^{-1}$ for the other lines. We have cautiously stopped the computation when

$I_{obs} \geq 2I_{corr}$, corresponding to an uncertainty in Ne of $\pm 30\%$.

The last step is to deconvolve the corrected zero-velocity columns for guiding errors and seeing by means of the profile, along the slit, of the stellar continuum present in the spectrum.

At each position of the zero-velocity column the intensity is proportional to $NeNi$ and, in the case of total ionization and $Te = \text{constant}$, $I \propto Ne^2$. This is valid, separately, for all ions.

As an example, the $H\alpha$ and $\lambda 6584 \text{ \AA}$ of [NII] zero-velocity columns derived at $PA=110^\circ$ (apparent minor axis) are presented in Figure 7; densities are normalized to the strongest peak (left ordinate scale). As expected, $Ne(H^+)$ and $Ne(N^+)$ practically coincide in the external parts (up to the maxima), and tend to diverge moving inwards, due to the gradual double ionization of nitrogen. Let's consider the H^+ curve; if we scale the western peak to $Ne=3100 \text{ cm}^{-3}$, as previously derived from the [SII] line intensity ratio (see Fig. 5), we obtain the true density distribution along the central, zero-velocity column (right ordinate scale). To be noticed that the density of the eastern peak results to be 2600 cm^{-3} , in fairly good agreement with the value derived from [SII] diagnostics.

In the same way we obtained the radial density trends at the other position angles; they are given in Figure 8. Note that the profiles observed at $PA=20^\circ$ correspond to the northern ($Ne=1000 \text{ cm}^{-3}$) and southern ($Ne=600 \text{ cm}^{-3}$) polar caps, and that only a weak emission ($Ne=400 \text{ cm}^{-3}$) is visible in the S-SE sector of $PA=155^\circ$.

In the end, the "bell" profile seems to be a general characteristic of the radial matter distribution within NGC 40.

A final note on the Ne problem in this nebula concerns [OII]. We have repeated the previous procedures using the 3726/3729 diagnostic ratio; the [OII] density trends are, in all cases, very close to the [SII] ones, but the actual density is systematically lower by a factor of almost two. To explain this curious feature, we must examine in detail the ionization structure of NGC 40.

5. Radial ionization structure

The detailed radial ionization structure of an expanding nebula can be derived by comparing the zero-velocity columns of different lines.

To obtain the ionic abundances (relative to H^+) of O^0 , O^+ , O^{++} , N^+ , C^+ , S^+ , He^+ and Ar^{++} we have applied the classical procedure (see, for instance, Peimbert and Torres-Peimbert, 1971; Barker, 1978; Aller and Czyzak, 1979, 1983).

For all ions, but not [ArIII], we have used the same atomic constants adopted by Clegg et al. (1983) in their low resolution study of NGC 40; for [ArIII], not mentioned by these authors, transition probabilities were taken from Mendoza (1983) and collision strengths from Galavis et al. (1995).

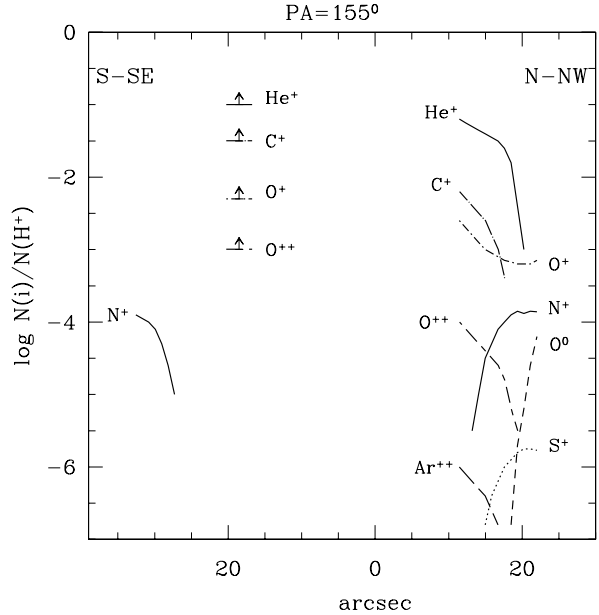


Fig. 9. Radial ionization structure of NGC 40 at $PA=155^\circ$ obtained from the zero-velocity columns. Details are given in the text.

Since the H^+ central column is practically absent in the S-SE sector of $PA=155^\circ$ (while other ions are present), only lower limits to the relative ionic abundances can be obtained; the same situation occurs at $PA=20^\circ$ (major axis), internally to the polar caps.

In all the remaining cases (where the radial ionization structure of the nebula can be studied in detail) most ions present the expected trends: medium-high ionization species (O^{++} , Ar^{++} , He^+) rapidly decrease outwards; the opposite for low ionization species, such as O^0 , N^+ and S^+ . Once again, O^+ shows an anomalous behavior (also C^+ has similar characteristics, but the CII $\lambda 6578 \text{ \AA}$ line is so weak that a quantitative analysis is hazardous).

The radial ionization structure of NGC 40 is synthesized in Figure 9 for $PA=155^\circ$; this position angle is a perfect compendium of the different situations occurring in the nebula, since it presents a well defined H^+ structure in the N-NW part and practically no hydrogen emission at S-SE (see Figure 8). Moreover, its N-NW peak corresponds to "position b" of Clegg et al. (1983), so that a direct comparison with their results can be made.

Let's first consider the N-NW sector of Figure 9; here both O^+/H^+ and O^{++}/H^+ increase inwards (while we would expect opposite trends, since the $O^+ \rightleftharpoons O^{++}$ equilibrium shifts on the left going outwards, so that when [OII] increases [OIII] falls, and vice versa). Note also that the O^{++} curve lies well below the O^+ one, indicating that the stellar flux is unable to completely ionize O^+ . Ionization structures similar (qualitatively and quantitatively)

to the one observed in the N-NW sector of PA=155⁰ were obtained at PA=65⁰ and 110⁰.

Look now at the left part of Figure 9. In the S-SE sector of PA=155⁰ the H⁺ zero-velocity column shows only a weak emission at about 30'' from the center (and here the N⁺/H⁺ trend was derived), whereas high ionization species are present also at intermediate positions, giving the lower limits to the He⁺/H⁺, C⁺/H⁺, O⁺/H⁺ and O⁺⁺/H⁺ abundances indicated in the figure. The degree of excitation in these hydrogen-depleted zones remains low, being N(O⁺)/N(O⁺⁺) ≥ 5. Similar low density, hydrogen-depleted regions are present at PA=20⁰ (major axis), internally to the polar caps.

An independent confirmation of the existence of a peculiar ionization structure in NGC 40 comes from the broad-band U, V and R imagery obtained with the 3.5m Italian National Telescope (TNG).

The R band (Figure 10 upper left) is dominated by H α and [NII], with a small contamination of [SII] at λ 6717 Å and λ 6731 Å.

Over 90% of the U light (Figure 10 upper right) comes from the [OII] doublet at λ 3726 Å and λ 3729 Å; the remaining is due to high Balmer lines.

Finally, in the V band (Figure 10 lower left) H β contributes for 55% and the [OIII] doublet at λ 4959 Å and λ 5007 Å for 45%.

Since the H β morphology of this low excitation planetary nebula is very similar to the H α + [NII] one, we can extract the [OIII] component of the V image by subtracting the R image (appropriately scaled in intensity) to the V image. The resulting [OIII] appearance of NGC 40, shown in Figure 10 lower right, noticeably differs from the H α + [NII] one; this morphological peculiarity, known since Louise (1981), stands out in great detail (greater than before; see, for instance, Balick, 1987 and Meaburn et al., 1996).

The apparent [OII]/[OIII] distribution over the nebula can be obtained from the ratio U/[OIII] and the (H α + [NII])/[OII] distribution from R/U; results are shown in Figures 11.

The large stratification effects present in these last maps indicate that all the three intensity ratios [OII]/[OIII], (H α + [NII])/[OII] and (H α + [NII])/[OIII] decrease inwards, i.e. all the three ionic ratios O⁺/O⁺⁺, (H⁺+N⁺)/O⁺ and (H⁺+N⁺)/O⁺⁺ decrease inwards. In conclusion: all the three ionic ratios O⁺⁺/O⁺, O⁺/H⁺ and O⁺⁺/H⁺ increase inwards (being the H⁺ distribution very similar to the N⁺ one). This is in perfect qualitative agreement with the results obtained from high resolution spectrography.

The obvious conclusions emerging from the peculiarities in the ionization structure of NGC 40 are drawn in the following, short section.

Fig. 10. Broad-band imagery of NGC 40 (seeing 0.85'') obtained with the 3.5m Italian National Telescope (TNG). The R image (upper left, exposure time 180s) is dominated by H α and [NII] and the U image (upper right, 600s) by the [OII] doublet at λ 3726 and λ 3729 Å. The V image (lower left, 180s) is the sum of H β (55%) and [OIII] at λ 4959 and λ 5007 Å (45%). The lower right panel shows the [OIII] appearance of NGC 40; it was obtained by subtracting the R image (appropriately scaled in intensity) to the V image.

Fig. 11. Left panel: apparent [OII]/[OIII] distribution in NGC 40. [OIII] is weak in the outermost strata (white), it gradually increases inwards, reaching its maximum (black) internally to the polar caps. Right panel: apparent (H α + [NII])/[OII] distribution in NGC 40. This intensity ratio presents a maximum (white) in the external, bright shell, it decreases inwards, and has a minimum (black) internally to the polar caps. Same orientation and scale as Fig. 10.

6. Abundance gradients towards NGC 40.

We believe that the radial ionization structure of NGC 40 indicates the presence of abundance gradients across the nebula (although we cannot exclude a minor effect due to electron temperature variations). Take oxygen, for instance.

The general expression O=O⁰+O⁺+O⁺⁺+etc. in the case of NGC 40 reduces to O=O⁺, i.e. the observed O⁺/H⁺ ratio is a good match of the total oxygen abundance. We obtain O/H=6±1 x10⁻⁴ in the main, denser regions (to be compared with the values of 6.0x10⁻⁴ and 8.4x10⁻⁴ given by Aller and Czyzak, 1983, and Clegg et al., 1983, respectively). O/H rapidly increases inwards; at the observational limit it is larger than 5x10⁻³.

Less accurate abundance gradients can be derived in a similar manner for C/H (1x10⁻³ to >3x10⁻²) and for He/H (4x10⁻² to >1x10⁻¹).

It is very tempting to attribute these abundance trends to contamination of the stellar wind (we remember that detailed analyses of the optical spectrum of the WC8 nucleus carried out by Leuenhagen et al., 1996, give an upper limit for the mass fraction of hydrogen of 2%; moreover, He/C=0.8 and C/O=5). In this scenario, our internal, low

density, hydrogen-depleted regions are essentially constituted of enriched material recently emitted by the central star. Moving outwards, this gas gradually mixes with the shell's gas and abundances rapidly fall to the nebular values.

The general expression $I \propto NeNi$ (valid in the zero velocity column) allows to estimate the electron density in the innermost, fast moving, hydrogen-depleted regions. An indicative value of 1 - 2 cm^{-3} is obtained, corresponding to a few 10^{-24} g cm^{-3} , and (for a distance of 1100 pc) to a matter flux of a few 10^{-8} $M_{\odot} \text{ yr}^{-1}$. This must be the order of magnitude of the present central star's mass-loss.

7. Tomography

In order to obtain the spatial matter distribution within a planetary nebula we will analyse the observed emission line structures by means of an iterative procedure which is the implementation of the method originally proposed by Sabbadin et al. (1985, 1987 and references therein) for plate echellograms. In this approach, the relative density distribution of an emitting region along the cross-section of nebula covered by the slit is obtainable from the radial velocity, FWHM and intensity profile.

The calibration to absolute densities is straightforward if [SII] or [OII] doublets are present (as in the case of NGC 40); for density bounded planetary nebulae other diagnostics (such as 5517/5537 of [CIII] or 4711/4740 of [ArIV]) can be used but, due to the intrinsic weakness of these lines, results are often uncertain; so, for high excitation planetary nebulae, we prefer to adopt the surface brightness method (it will be described in a forthcoming paper dedicated to NGC 1501).

The tomographic analysis contains a large amount of physical informations; for reasons of space too, this first application to NGC 40 intends to be a concise test of reliability (i.e. a semi-quantitative comparison with the observational results independently accumulated in the previous sections).

Amongst the different maps (intensity, density, fractional ionization, ionic abundance etc.) obtainable with our reconstruction method, we have selected \sqrt{NeNi} ; H^+ was chosen as ionization marker, and N^+ and O^{++} to symbolize low and high excitation zones, respectively.

Since for H^+ we have that \sqrt{NeNi} is proportional to Ne , the H^+ maps give the relative density distributions along the cross-sections of NGC 40 covered by the slit; this is roughly true also for N^+ (its ionization occurring only in the innermost parts), but not for O^{++} , due to the incomplete O^+ ionization.

The gray-scale \sqrt{NeNi} maps derived for H^+ , O^{++} and N^+ at PA=110°, 20°, 65° and 155° are shown in Figure 12.

At PA=110° (apparent minor axis) H^+ describes a circular, knotty ring; N^+ closely mimics H^+ (but, obviously, it is a bit sharper), while O^{++} is emitted in the internal

regions and rapidly drops when Ne raises. To be noticed the opposite behaviors of H^+ and O^{++} , in the sense that bright H^+ zones tend to be associated with faint O^{++} regions, and vice versa; the patch studied by Clegg et al. (1983, their "position a") corresponds to our western edge.

At PA=20° (apparent major axis) the H^+ and N^+ ring structures appear disrupted at north and south, where the two polar caps are formed; unfortunately, in these reproductions we have lost the two extremely faint (and fast moving) low excitation mustaches attached to the main nebular body (blue-shifted at north, red-shifted at south). The elliptical structure shown at this position angle by O^{++} testifies the existence of hydrogen-depleted zones internally to the polar caps (which, in our opinion, are essentially constituted of stellar wind).

The Ne map derived from H^+ at PA=65° describes a distorted ring presenting a deformation in the approaching gas of the E-NE quadrant; the bright knots visible in both the H^+ and N^+ maps completely disappear in the O^{++} one, which presents a more homogeneous distribution.

Finally, at PA=155° the ring structure shown by H^+ and N^+ in the N-NW sector is completely absent at S-SE; once again, O^{++} indicates the presence of hydrogen-depleted gas within the S-SE region; the N-NW border corresponds to "position b" of Clegg et al. (1983).

Quantitative maps, giving the true electron density distribution at the four position angles, can be obtained by calibrating the H^+ maps of Fig. 12 with the [SII] line intensity ratio. Results are shown in Figure 13, where the nebular centre corresponds to the position of the exciting star (which, actually, lies 2'' over or below the plane of the figure).

8. Discussion

The general rule given by Olin Wilson (1950) in his classical work on the expansion velocity of planetary nebulae -"high-excitation particles show smaller separation, and low-excitation particles higher separation"- is definitely violated in NGC 40, which presents a positive inwards velocity gradient. Moreover, this velocity gradient is small enough ($\Delta V \simeq 3 - 4$ km s^{-1} for the main shell) to rouse the suspicion that some nebular lines can be produced by resonance scattering.

The problem has been analysed in detail by Clegg et al. (1983), who tried to explain the abnormal CIV $\lambda 1549$ Å intensity observed in NGC 40 in terms of stellar light scattered by the nebula. Assuming a spread in velocity of 20 km s^{-1} , these authors obtained that the stellar flux at $\lambda 1549$ Å is nine times larger than the $\lambda 1549$ Å nebular scattered flux and concluded that scattering is inadequate, but pointed out that "this mechanism will be most effective if velocity gradients are small". Decidedly, our new ΔV value re-opens the question.

We have seen that the peculiarities found in the ionization structure strongly suggest the presence of abundance

Fig. 12. Gray-scale \sqrt{NeNi} spatial maps of NGC 40 in H^+ (left), O^{++} (center) and N^+ (right) at different position angles. For H^+ we have that \sqrt{NeNi} is proportional to Ne; this is approximately valid also for N^+ , due to the very low degree of excitation of the nebula, but not for O^{++} , since the O^+ ionization is incomplete .

Fig. 13. Isophotal density maps of NGC 40 obtained from H^+ . Contour levels: dashed curve=250 cm^{-3} , solid curves=500, 1000, 1500, 2000, 2500, 3000 and 3500 cm^{-3} . Same orientation as Fig. 12. In each map the central star is located $2''$ over or below the plane of the figure .

gradients within NGC 40; the responsible of these gradients is the fast stellar wind. This is not a surprise since, following Bianchi and Grewing (1987), the mass of the central star is close to the C-O core of the progenitor star.

It is interesting to note the discrepancy found by these authors between the stellar temperature determined from IUE observations (90000 K) and the much lower value of 30000 K inferred from the nebular ionization. They overcame the impasse with a carbon curtain screening the high energy photons; this $2 - 5 \times 10^{18} cm^{-2}$ CII column density should be located at the inner edge of the shell, where the fast wind from the nucleus interacts with the nebular gas.

The hypothesis is suggestive, but some doubts remain, essentially for lack of space. In fact, on one side our ionization maps indicate that the CII layer producing the requested column density must have a thickness of the order of $10^{19} cm$, on the other side the mean nebular radius of NGC 40 (assuming a distance of 1100 pc, centre of the large number of individual and statistical distances reported in the literature) is 0.08 pc, i.e. 40 times shorter than the CII layer. An even more unfavorable situation occurs for a nebular distance of 980 pc, as adopted by Bianchi and Grewing (1987).

We wish to stress here the great opportunities opened by the analysis of the zero-velocity columns in expanding nebulae (planetary nebulae, shells around Population I W-R stars, supernova remnants etc.): for the first time we can insulate a definite slide of nebula, thus removing the tiresome projective problems related to these extended objects.

To be noticed the strict analogy between the zero-velocity column obtained from slit spectroscopy and the rest-frame image derived from Fabry-Perot interferometry; in a certain sense, the rest-frame image is a zero-velocity column extended at all position angles (and this represents a considerable observational advantage).

Moreover, the expansion velocity of a few objects (for instance the Crab nebula) is so large that the “zero-velocity column” analysis can be applied to very low resolution data (slit spectroscopy or Fabry-Perot interferometry).

Concerning our tomographic results, we confess a genuine satisfaction for the quality of these “preliminary” maps (clearly, the final goal of each tomographic study is a complete, three-dimensional model, but this will need a more detailed spectroscopic coverage).

Our figures confirm that the main body of NGC 40 has an inhomogeneous, elongated barrel-shaped structure (“an opened-up ellipse” following Mellema, 1995; “a slightly tilted cylindrical sleeve” following Balick et al., 1987), with thin arcs emerging at both ends of the major axis.

This morphology is normally interpreted as the result of the interaction of the fast stellar wind from the high temperature central star with the slow, inhomogeneous (i.e. denser in the equatorial plane) super-wind from the AGB progenitor (see Balick et al., 1987, Mellema, 1995 and references therein).

Following Balick et al. (1987) the stellar wind creates in NGC 40 an interior bubble at high temperature and ionization. The hot gas cools by expansion or radiative losses in forbidden lines when it interacts with the dense, external shell; [OIII] emissions arise in a relatively smooth, low density interface between the bubble gas and the $H\alpha + [NII]$ filaments.

As noticed by Meaburn et al. (1996), in this case the [OIII] image is expected to follow the $H\alpha + [NII]$ one, and both are dominated by the swept-up shell. The alternative explanation proposed by Meaburn et al. is based on Mellema’s (1995) models: the nebular material is swept-up both by the fast wind and by the ionization front. So, in the first evolutionary phases, when the central star temperature is still relatively low, the two shells appear as

distinct features: $H\alpha$ and [NII] prevail in the shell swept-up by the H ionization front, and [OIII] in the wind-swept shell. In the specific case of NGC 40, the second, faster shell has almost undertaken the first one.

Which model is right? The answer provided by our data is ambiguous: on one side we obtain that the [OIII] and the $H\alpha$ + [NII] emitting regions are disconnected (in many cases they are opposite, i.e. strong [OIII] is associated with faint $H\alpha$ + [NII], and vice versa); on the other side the density distribution across the shell never shows evidence of a double peaked structure implicit in Mellema's models.

So, for the present, we can only say that:

- in the equatorial region of NGC 40 the stellar wind is blocked by the dense nebular gas and [OIII] emissions occur in the innermost, faster expanding part of the "bell" density profile;

- at the poles, where densities are lower than at the equator, the braking effect by the nebular gas is less efficient and [OIII] appears in extended zones, internally to the polar caps.

A question arises: since we observe modest expansion velocities in the nebular gas, where (and how) is decelerated the stellar wind, whose original speed is of about 2000 km s^{-1} ?

It is evident that further, more accurate observations are needed not only for the nebula, but also for the central star. At the moment, mass-loss rates and terminal wind velocities reported in the literature for the WC8 nucleus of NGC 40 span in the range $3 \times 10^{-8} M_{\odot} \text{ yr}^{-1}$ and 2600 km s^{-1} (Cerruti-Sola and Perinotto, 1985) to $1 \times 10^{-6} M_{\odot} \text{ yr}^{-1}$ and 1800 km s^{-1} (Bianchi, 1992). Moreover, the presence of wind fluctuations was recently discovered by Balick et al. (1996) and Acker et al. (1997).

The ionized nebular mass obtained from the observed $H\beta$ flux (Sabbadin et al., 1987) results to be $M_{ion} = 2 - 5 \times 10^{-2} M_{\odot}$ (depending on the adopted values of $F(H\beta)$, $c(H\beta)$, distance, angular radius, electron density and electron temperature), and a conservative upper limit to the nebular mass pumped up by the fast stellar wind can be put at $1 \times 10^{-2} M_{\odot}$.

Even in the most favorable case (i. e. momentum conservation), Bianchi's wind ($10^{-6} M_{\odot} \text{ yr}^{-1}$ and 1800 km s^{-1}) needs less than 20 years to produce the observed nebular acceleration (and in this case, where, and how, is dissipated the wind luminosity, amounting to $500 L_{\odot}$, a value which is at least ten times the nebular luminosity?).

A longer interaction time (500 years) is obtained with the mass-loss rate and wind velocity reported by Cerruti-Sola and Perinotto (1985); in this case the wind luminosity is $33 L_{\odot}$, of the same order of magnitude of the nebular luminosity.

A final question concerns NGC 40 as prototype of a small group of very low excitation planetary nebulae powered by "late" WR stars: are the peculiarities found in NGC 40 (in particular, the positive inwards velocity

gradient and the radial chemical composition gradient) a common characteristic of these nebulae (e. g. SwSt 1, PM 1-188, Cn 3-1, BD+30°3639, He 2-459, IRAS 21282, M 4-18, He 2-99, He 2-113, He 2-142, He 3-1333, Pe 1-7 and K 2-16)?

Though a definitive answer will need accurate imagery and spectroscopy of a suitable sample of objects, a first indication comes from the very recent results by Bryce and Mellema (1999), showing that BD+30°3639 expands faster in [OIII] than in [NII].

9. Conclusions

Long-slit echellograms at different position angles of the bright core of NGC 40 allowed to analyse the expansion velocity field (the higher is the ionization, the faster is the motion), the radial density distribution (a "bell" profile reaching $N_e=4000 \text{ cm}^{-3}$), the radial ionization structure (peculiar in the innermost parts), and the chemical abundances (a gradient is present, due to contamination of the hydrogen-depleted stellar wind).

Moreover, tomographic maps are obtained, giving the spatial matter distribution along the cross-sections of nebula covered by the slit.

All these observational results, discussed within the interacting winds model, point out our incomplete, "nebulous" knowledge of the physical processes shaping this peculiar planetary nebula where "the tail wags the dog" (as wittily suggested by Prof. Lawrence Aller, private communication).

Acknowledgements. We wish to express our gratitude to Professors Lawrence Aller and Manuel Peimbert and to Drs. Luciana Bianchi, Francesco Strafella and Vittorio Buondì for help, suggestions and encouragements.

We thank the whole technical staff -in particular the night assistants- of the Astronomical Observatory of Asiago at Cima Ekar for their competence and patience.

This paper is partially based on observations made with the Italian Telescopio Nazionale Galileo (TNG) operated on the island of La Palma by the Centro Galileo Galilei of the CNAA (Consorzio Nazionale per l'Astronomia e l'Astrofisica) at the Spanish Observatorio del Roque de los Muchachos of the Instituto de Astrofísica de Canarias.

References

- Acker A., Grosdidier Y., Durand S., 1997, A&A, 317, L51.
- Acker A., Ochsenbein F., Stenholm B., Tylenda R., Marcourt J., Schohn C., 1992, Strasbourg-ESO Catalogue of Galactic Planetary Nebulae. ESO, Garching.
- Aller L.H., Czyzak S.J., 1979, Ap&SS, 62, 397.
- Aller L.H., Czyzak S.J., 1983, ApJS, 51, 211.
- Balick B., 1987, AJ, 94, 671.
- Balick B., Bignell C.R., Hjellming R.M., Owen R., 1987, AJ, 94, 948.
- Balick B., Gonzalez G., Frank A., Jacoby G., 1992, ApJ, 392, 582

- Balick B., Rodgers B., Hajian A., Terzian Y., Bianchi L., 1996, *AJ*, 111, 834.
- Barker T., 1978, *ApJ*, 193, 209.
- Bianchi L., 1992, *A&A*, 253, 447.
- Bianchi L., Grewing M., 1987, *MNRAS*, 181, 85.
- Bryce, M., Mellema, G., 1999, *MNRAS*, 309, 731.
- Brocklehurst M., 1971, *MNRAS*, 153, 471.
- Cerruti-Sola M., Perinotto M., 1985, *ApJ*, 291, 237.
- Clegg R.E.S., Seaton M.J., Peimbert M., Torres-Peimbert S., 1983, *MNRAS*, 205, 417.
- Curtis H.D., 1918, *Publ. Lick Obs.*, 13, 55.
- Dopita M., 1972, *A&A*, 17, 165.
- Dyson J.E., Meaburn J., 1971, *A&A*, 12, 219.
- Galavis M.E., Mendoza C., Zeippen C.J., 1995, *A&AS*, 111, 347.
- Kaler J.B., 1976, *ApJS*, 31, 517.
- Leuenhagen U., Hamann W.-R., Jeffery C.S., 1996, *A&A*, 312, 167.
- Louise R., 1981, *A&A*, 102, 303.
- Meaburn J., Lopez J.A., Bryce M., Mellema G., 1996, *A&A*, 307, 579.
- Mellema G., 1995, *MNRAS*, 277, 173.
- Mendoza C., 1983, in *Planetary Nebulae*, IAU Symp. N. 103, ed. D.R. Flower. Reidel, Dordrecht, p. 143.
- Peimbert M., Torres-Peimbert S., 1971, *ApJ*, 168, 413.
- Sabbadin F., Bianchini A., Ortolani S., Strafella F., 1985, *MNRAS*, 217, 539.
- Sabbadin F., Cappellaro E., Turatto M., 1987, *A&A*, 182, 305.
- Sabbadin F., Hamzaoglu E., 1981, *MNRAS*, 197, 363.
- Sabbadin F., Hamzaoglu E., 1982, *A&A*, 109, 131.
- Wilson O., 1950, *ApJ*, 111, 279.

This figure "ms9009f1.jpg" is available in "jpg" format from:

<http://arxiv.org/ps/astro-ph/9912040v1>

This figure "ms9009f2a.jpg" is available in "jpg" format from:

<http://arxiv.org/ps/astro-ph/9912040v1>

This figure "ms9009f2b.jpg" is available in "jpg" format from:

<http://arxiv.org/ps/astro-ph/9912040v1>

This figure "ms9009f2c.jpg" is available in "jpg" format from:

<http://arxiv.org/ps/astro-ph/9912040v1>

This figure "ms9009f2d.jpg" is available in "jpg" format from:

<http://arxiv.org/ps/astro-ph/9912040v1>

This figure "ms9009f10.jpg" is available in "jpg" format from:

<http://arxiv.org/ps/astro-ph/9912040v1>

This figure "ms9009f11.jpg" is available in "jpg" format from:

<http://arxiv.org/ps/astro-ph/9912040v1>

This figure "ms9009f12.jpg" is available in "jpg" format from:

<http://arxiv.org/ps/astro-ph/9912040v1>

This figure "ms9009f13.jpg" is available in "jpg" format from:

<http://arxiv.org/ps/astro-ph/9912040v1>